CHAPTER-4

Development and evaluation of electrochemical performance of cobalt tungstate $Co_xW_{2-x}O_4$; x = 0.5, 1.0, 1.5 catalysts for alkaline water oxidation: Tailoring composition for optimal activity

4.1. Abstract

The creation of effective and affordable water oxidation catalysts is a major obstacle to enhance the performance of large-scale energy solutions based on electricity-driven hydrogen generation from water. Significant attempts were made to increase the catalytic efficiency of electrocatalysts derived from 3D-transition metals, particularly those based on cobalt, which are seen to be viable options for non-noble catalysts in electrocatalytic water splitting. In the present article, we have synthesized various stoichiometries of cobalt tungstate via a one-pot hydrothermal method. The prepared catalysts were then thoroughly characterized by XRD, FT-IR, Raman Spectroscopy, HR-TEM, and XPS. Afterwards, electrochemical studies like LSV, CV, EIS, and Tafel polarization analysis were done to test the potential of the electrocatalysts for oxygen evolution reaction (OER) in basic environment. Among the various stoichiometries, the lowest overpotential was found to be 220 mV for $CoWO_4$ to provide 10 mA cm^{-2} current density (η_{10}), which is better than the benchmarking IrO_2 (313 mV). Further, it has the lowest R_{ct} and Tafel slope of 56 Ω and 75 mV dec^{-1}, respectively among other prepared catalysts.

4.2. Introduction

The environment and the people, both have suffered as a result of the quick depletion of fossil fuels [1]. To generate energy on a wide scale and at a low cost, clean and sustainable alternatives must be developed [2]. In this regard, electrochemical technologies like water splitting, fuel cells, and batteries will successfully lessen the effects of environmental degradation and the fossil fuel crisis [3,4]. As a clean, effective, and sustainable energy source, hydrogen is becoming increasingly important in the shift to a low-carbon future [5,6]. The

electrochemical conversion of H_2O into H_2 and O_2 is important because of its relevance to energy conversion [7,8].

The two half-cell processes that make up water electrolysis are cathodic hydrogen evolution (HER) and anodic oxygen evolution (OER) [9,10]. In contrast to HER, OER is kinetically poor and occurs at far higher overpotentials [11,12], which encourages researchers to look for active catalysts with significantly lower overpotentials [13,14]. The best electrocatalysts for OER at present, are precious metal oxides such as RuO_2 and IrO_2 [15–17], because of their favorable binding energy with reaction intermediates (*OH, *O, and *OOH), but their high cost and limited availability prevent their widespread use. To increase the electrolysis process's efficiency, efforts are still being made to find inexpensive, effective, and thermodynamically stable OER electrode materials.

Numerous affordable materials have been created as sophisticated OER electrocatalysts as a result of the enormous efforts put forward. Transition metal hydroxides and oxides have garnered increased attention among different electrocatalysts because of their compositional benefits; yet, because of their weak conductivity and unsatisfactory electronic structure, they also require a high overpotential to achieve a desired current density [18,19]. Consequently, it is essential to alter the electronic structure of transition metal oxides and enhance their electrical conductivity to improve catalytic performance. As demonstrated for Te-doped materials [20,21], such electronic modulation can significantly enhance activity. We have employed a similar manner to achieve comparable improvements in conductivity and catalytic behavior.

WO_3 exhibits a reversible surface oxygen ion exchange aptitude and an exceptional oxygen storage capacity to facilitate reactant activation because of the multi-valence oxidation states of W (W^{6+}, W^{5+}, and W^{4+}) [22]. Notably, of all the tungsten oxides, hexavalent tungsten oxide (WO_3) is extremely reliable [23]. According to studies, WO_3's oxygen vacancies alter its electronic framework to increase its electrocatalytic functionality in addition to enhancing its electrical conductivity [24,25]. A few numbers of research employing WO_3 as an electrocatalytically operational component for OER have been published thus far. Because of the sluggish charge transfer at the WO_3/water interface, pure WO_3 continues to perform inadequately in OER [26]. Since CoO_x nanoparticles are well-known for being superior water oxidation catalysts, sub-nano cobalt oxide catalysts are applied to the WO_3 surface. With a dramatically better current density and a 13-fold rise in OER activity, the Co-modified WO_3 significantly improved the performance of WO_3 in OER [27]. Because of their exceptional physio-chemical characteristics, including superior electrochemical activity, good stability, low level of toxicity, affordability, environmental friendliness, and earth abundance, metal tungstites MWO_4 (where M = Co, Ni, Zn, Mn, Cu, etc.) have been regarded as promising electrode materials for OER [28,29].

By varying metal stoichiometries, we could optimize and greatly increase the stability and boost OER efficiency. In the present study, we have synthesized $Co_xW_{2-x}O_4$ (x= 0.5, 1.0, 1.5) via a one-pot hydrothermal method. The prepared catalysts were gone through various physicochemical techniques like XRD, FTIR, Raman Spectroscopy, HR-TEM, and XPS to fully investigate the morphology and structure of these materials. Further, a thorough

assessment of the electrocatalytic efficacy of the prepared electrocatalysts was conducted in 1 M KOH solution.

4.3. Experimental

4.3.1. Materials

Cobalt chloride hexahydrate ($CoCl_2 \cdot 6H_2O$) (AR, Merck, 99.9 %), sodium tungstate dihydrate ($Na_2WO_4 \cdot 2H_2O$) (AR, Merck, 99.9 %), sodium hydroxide (NaOH) (AR, Merck, 99.9 %), ethanol (99.9 %), and double distilled water. All the chemicals were applied just as they were delivered, without any further processing or refining.

4.3.2. Preparation of $Co_xW_{2-x}O_4$

The cobalt tungstate nanomaterials were synthesized using a hydrothermal approach. Initially, two precursor solutions were prepared by taking stoichiometric amounts of sodium tungstate dihydrate ($Na_2WO_4 \cdot 2H_2O$) and cobalt chloride hexahydrate ($CoCl_2 \cdot 6H_2O$), dissolved in 15 mL of deionized water separately **(Table 4.1)**. These solutions were then combined under continuous stirring, leading to the formation of a thick red colored suspension. The pH of the reaction mixture was carefully maintained to 8 using sodium hydroxide (NaOH) solution, added dropwise under vigorous stirring to ensure uniformity. The resulting homogeneous solution was transferred into a 50 mL Teflon-lined stainless-steel autoclave and underwent heating hydrothermally at 160 °C for 24 hours to facilitate controlled crystallization of $Co_xW_{2-x}O_4$. After completion of the reaction, the precipitated product was collected and thoroughly washed repeatedly with double distilled water and ethanol to eliminate any remaining

impurities or unreacted species. At last, the purified material was dried at 120 °C for 6 hours to obtain the desired $Co_xW_{2-x}O_4$ catalyst.

Table 4.1. Required stoichiometric amounts of metal precursors used for the synthesis of cobalt tungstate nanoparticles.

Catalysts	($Na_2WO_4 \cdot 2H_2O$)		($CoCl_2 \cdot 6H_2O$)	
	No. of mmol	Amount (g)	No. of mmol	Amount (g)
$Co_{0.5}W_{1.5}O_4$	1.5	0.495	0.5	0.119
$CoWO_4$	1.0	0.330	1.0	0.238
$Co_{1.5}W_{0.5}O_4$	0.5	0.165	1.5	0.357

4.3.3. Electrode fabrication

For preparing the ink of catalyst, 1 mg of the synthesized catalyst was dispersed in a solvent consisting of 20 µL deionized water, 40 µL ethanol, and 10 µL of a 5 % Nafion. This mixture was subjected to ultrasonication for 1 hour to achieve a homogeneous dispersion, ensuring uniform distribution of catalyst particles within the solution. Following the ink preparation, 60 µL of the well-dispersed suspension was carefully drop-casted onto pre-cleaned FTO glass substrates, each with a dimension of 1 × 1 cm^2. The coated electrodes were then left to dry at

ambient temperature, allowing solvent evaporation and the formation of a uniform catalytic film. These prepared FTO coated electrodes were subsequently utilized as working electrodes for electrochemical analysis.

4.4. Characterizations

4.4.1. Physicochemical characterizations

A comprehensive suite of analytical techniques was employed to investigate the morphological, structural, vibrational, and elemental composition of the prepared cobalt tungstate catalysts. The samples were analyzed to determine their phase composition and crystalline structure using X-ray diffraction (XRD) patterns, recorded on a Rigaku Smart Lab 9 kW diffractometer with a wavelength of 1.514 Å. The diffraction patterns were recorded over a 2θ window of 10° to 90°, with a scan rate of 4° min^{-1}. The vibrational characteristics and functional groups present in the $CoWO_4$ samples were examined using Fourier transform infrared (FTIR) spectroscopy. The spectra were acquired in the wavenumber range of 500–4000 cm^{-1} using the ATR-FTIR (Bruker, ALPHA model) spectrophotometer. Raman spectroscopic measurements were conducted to further probe the vibrational modes and structural properties of the samples. The spectra were collected at room temperature over a wavenumber range of 150–1000 cm^{-1} using a Raman spectrometer α-300, AFM SNOM. The particle size, morphology, and structural integrity of the $CoWO_4$ catalyst were investigated using high resolution transmission electron microscopy (HR-TEM). The TEM micrographs were captured using a Thermo Fisher Technai 20 G^2 microscope. The elemental composition

and chemical states of the $CoWO_4$ samples were identified using X-ray photoelectron spectroscopy (XPS). The spectroscopic analysis was performed on a K-alpha XPS equipment.

4.4.2. Electrochemical characterizations

Electrochemical evaluation of the prepared materials was conducted employing a three-electrode system at room temperature. All electrochemical assessments were conducted on a CHI-608C electrochemical workstation manufactured by CH Instruments, USA. A high-purity (99.9 %) circular platinum (Pt) foil having exposed surface area of 8 cm^2, procured from Aldrich, was employed as the counter electrode. The working electrode consisted of fluorine-doped tin oxide (FTO) coated glass plates with an active area of 0.50 cm^2, onto which the electrode material was deposited. A Hg/HgO electrode, immersed in a 1 M KOH electrolyte solution, was utilized as the reference electrode to maintain a stable electrochemical potential. The electrochemical activity of the synthesized materials was systematically analyzed using electrochemical impedance spectroscopy (EIS), linear sweep voltammetry (LSV), and cyclic voltammetry (CV). EIS measurements were performed to assess charge transfer resistance. These experiments were carried out over a wide frequency range, spanning from 10 mHz to 100 kHz. A perturbation of 5 mV was applied during the EIS measurements to ensure accurate impedance characterization. In this study, all measured electrochemical potentials were referenced against the Hg/HgO electrode in 1 M KOH. The standard potential of the Hg/HgO reference electrode ($E^0_{Hg/HgO}$) is 105.3 mV vs. NHE. **Equation 3.1** could be used for converting the potential to RHE scale, which is already discussed in **Chapter 3**.

$$E_{RHE} = E_{Hg/HgO} + 0.0592 \times pH + E^0_{Hg/HgO} \qquad \textbf{(3.1)}$$

4.5. Results and discussion

4.5.1. Physicochemical characterizations

4.5.1.1. XRD

Figure 4.1 illustrates the XRD data of the three prepared cobalt tungstate ($Co_xW_{2-x}O_4$) samples. The diffraction patterns confirm that all three materials adopt a monoclinic crystal structure characteristic of the wolframite-type phase. At 2θ values of 15.5°, 18.9°, 23.7°, 24.6°, 30.6°, 36.3°, 38.4°, 41.2°, 44.3°, 45.7°, 52°, 53.9°, 61.7°, 65.1°, 68.6°, and 71.8°, the diffraction peaks for $CoWO_4$ were visible corresponding to (010), (001), (−110), (011), (−111), (200), (002), (−201), (−211), (−112), (031), (−202), (−311), (−231), (−140), and (−312) crystal planes, respectively. These values exhibit strong agreement with previously reported data in the literature, particularly those documented in references [30,31], as well as in the standard reference files from JCPDS file no. 15-0867. A crucial observation from the XRD analysis is the absence of additional diffraction peaks corresponding to unreacted precursor materials, indicating that the synthesized $Co_xW_{2-x}O_4$ samples are phase-pure.

The Debye-Scherrer equation **(Equation 3.2),** which is already discussed in **Chapter 3**, was utilized to ascertain the crystallite size (D) of the prepared catalysts. This offers essential assessment on the structural characteristics of the synthesized nanoparticles by connecting the average crystallite size to the widening of diffraction peaks in the XRD pattern. A quantitative assessment of the nanoscale characteristics of the as-prepared samples was provided by estimating the crystallite size by examining the full width at half maximum (FWHM) of the intense diffraction peak.

$$D = \frac{k\lambda}{\beta \cos\theta} \qquad \textbf{(3.2)}$$

Where, the X-ray wavelength is represented by λ,

β denotes the full width at half maximum (FWHM) of the diffraction peak,

θ corresponds to the Bragg's angle,

The Scherrer constant (k), which accounts for the shape of the crystalline domains, is taken as 0.89, as commonly adopted in the literature [32].

Based on this calculation, the average crystallite size was determined to be approximately 22.40 nm, 19.51 nm, and 26.19 nm for $Co_{0.5}W_{1.5}O_4$, $CoWO_4$, and $Co_{1.5}W_{0.5}O_4$, respectively.

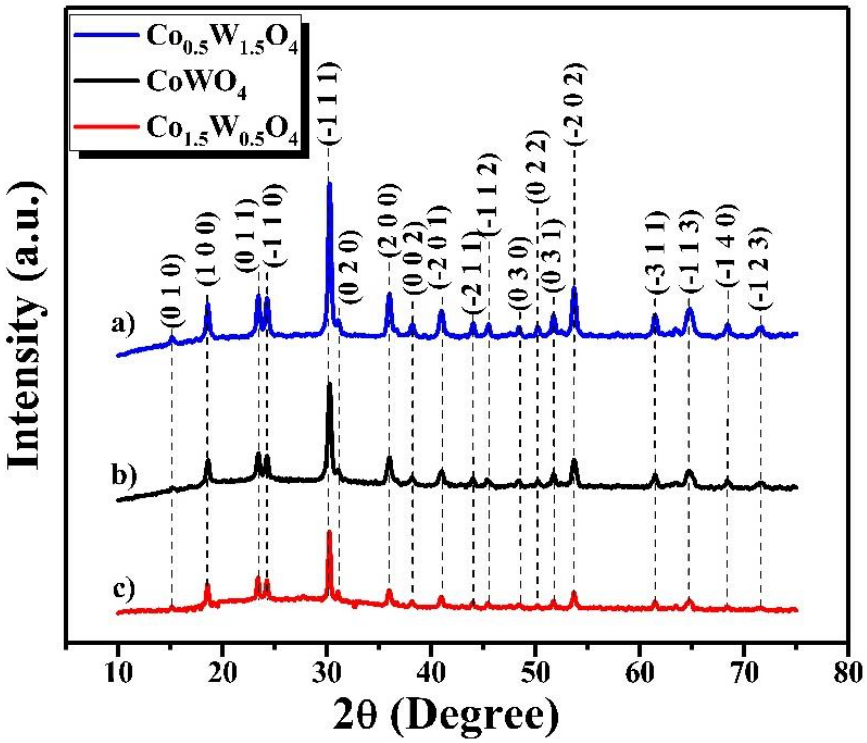

Figure 4.1. XRD patterns of **a)** $Co_{0.5}W_{1.5}O_4$, **b)** $CoWO_4$, **c)** $Co_{1.5}W_{0.5}O_4$.

4.5.1.2. FT-IR

An effective analytical method for examining the vibrational properties of synthetic materials is the FT-IR, recorded in the 400–4000 cm^{-1} spectral region. The FT-IR spectra of the cobalt tungstate ($Co_xW_{2-x}O_4$) as synthesized and its other two stoichiometries are shown in **Figure 4.2**. Different vibrational modes that correlate to the bonding interactions found in the synthesized materials are shown by the spectra. The stretching vibrations of the Co–O–W mode are responsible for the noticeable wide band at around 624 cm^{-1}, whilst the O–Co–W–O stretching vibration is responsible for the peak at 804 cm^{-1} [33]. Additionally, the W=O=Co stretching vibration is identified by a distinctive band at 1636 cm^{-1}. The stretching vibrations of hydroxyl (-OH) groups are linked to a relatively wider band at around 3370 cm^{-1}, which clearly shows the existence of water molecules in the produced samples [28]. This implies that the materials' propensity to absorb ambient moisture persists even after annealing.

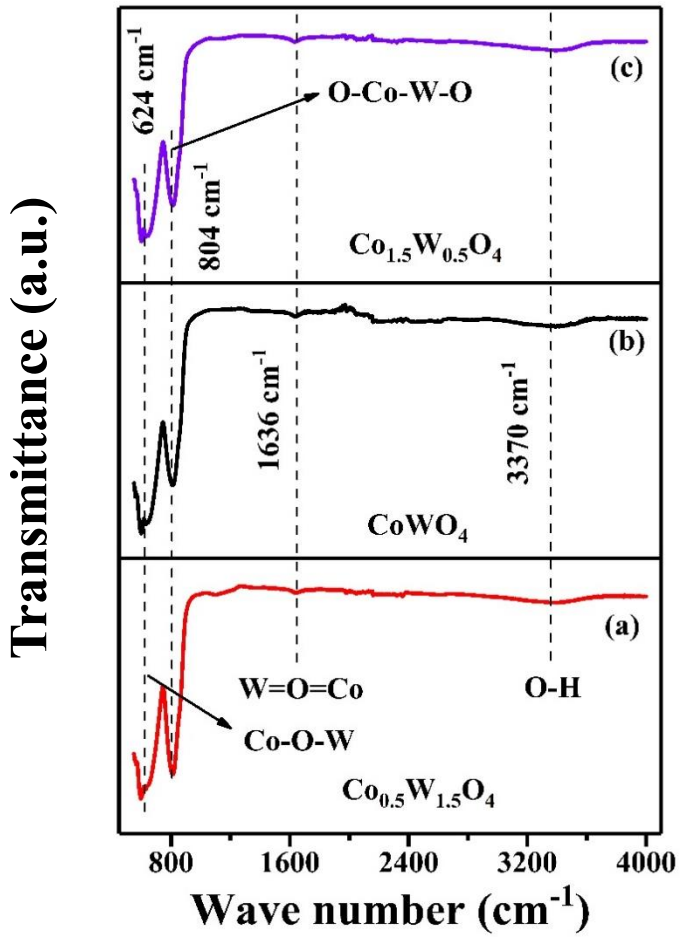

Figure 4.2. FT-IR of **(a)** $Co_{0.5}W_{1.5}O_4$, **(b)** $CoWO_4$, **(c)** $Co_{1.5}W_{0.5}O_4$.

4.5.1.3. Raman Spectroscopy analysis

Raman spectroscopy is acknowledged as an effective and non-destructive analytical method for examining the structural order and disorder in crystalline materials. This technique offers essential insights into the vibrational properties of synthesized samples. **Figure 4.3** illustrates the Raman spectra of cobalt tungstate ($Co_xW_{2-x}O_4$), emphasizing the unique vibrational characteristics of each material. The spectra exhibit a prominent peak at 885 cm^{-1}, along with several medium-intensity bands at 770 cm^{-1}, 690 cm^{-1}, 539 cm^{-1}, 408 cm^{-1}, 339 cm^{-1}, 277

cm^{-1}, 210 cm^{-1}, 190 cm^{-1}, 161 cm^{-1}, 134 cm^{-1}, and 94 cm^{-1}. The observed peaks align with the characteristic vibrational modes of $CoWO_4$, corroborating previously reported findings [34].

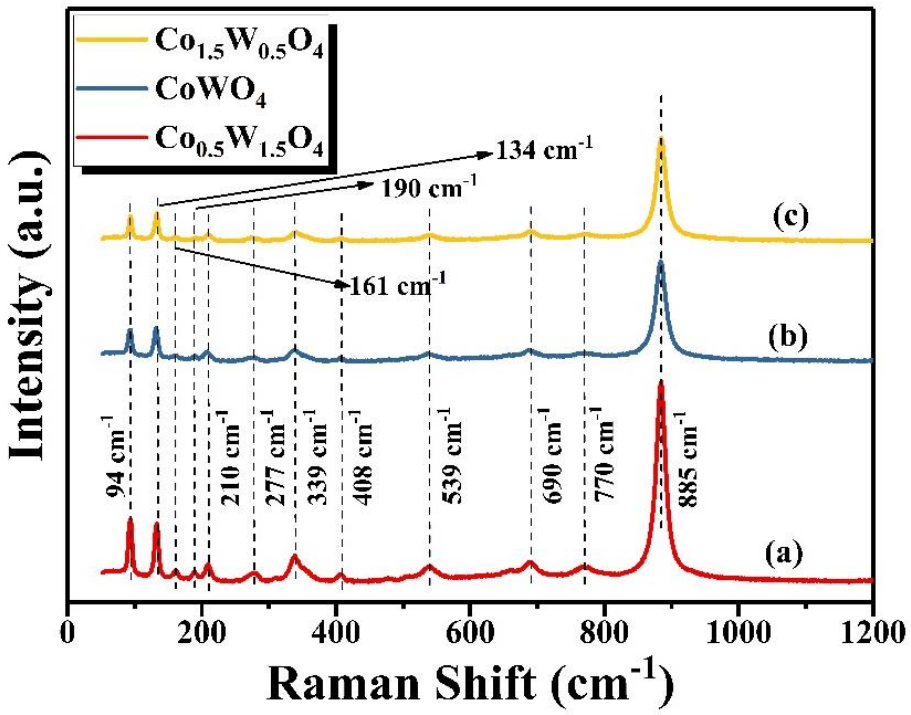

Figure 4.3. Raman spectra of **(a)** $Co_{0.5}W_{1.5}O_4$, **(b)** $CoWO_4$, **(c)** $Co_{1.5}W_{0.5}O_4$.

The peaks at 885 cm^{-1} and 770 cm^{-1} are associated with the symmetric and asymmetric stretching vibrations of the W=O bond, comparable to similar modes reported for $ZnWO_4$ and $CdWO_4$ [35,36]. Weak bands identified at 690, 539, and 408 cm^{-1} correspond to the Co-O bond [37]. Additionally, the peak at 339 cm^{-1} is attributed to the moderate scissoring motion of WO_2 as well as W-O-W [37]. The Raman peak observed at 210 cm^{-1} is likely associated with an out-of-plane vibrational mode, reflecting structural distortions within the lattice. Additionally, a weak band detected at 277 cm^{-1} is attributed to the bending vibrational mode of the octahedral $[WO_6]^{6-}$ units. The lower-frequency bands at 134, 161, and 190 cm^{-1} are associated with

interchain torsional deformation modes, which enhance the structural flexibility of the material [38,39]. Finally, the band at 102 cm^{-1} corresponds to lattice vibrations, reflecting the intrinsic structural dynamics of the synthesized material [40].

4.5.1.4. HR-TEM

The structural and morphological features of the prepared cobalt tungstate ($CoWO_4$) nanoparticles were examined using TEM, as depicted in **Figure 4.4**. The TEM image **(Figure 4.4 (a))** reveals that $CoWO_4$ nanoparticles exhibit a nearly spherical morphology, with particle size distributed in the range of approximately 20-60 nm. Further structural insights were obtained from HR-TEM and SAED patterns. The SAED image **(Figure 4.4 (b))** display a combination of both spot and ring diffraction patterns, indicating the polycrystalline nature of the synthesized tungstate material. The HR-TEM analysis **(Figure 4.4 (c))** reveals well-defined lattice fringes with determined interplanar spacings of 0.42 nm and 0.50 nm, which correspond closely to the d-spacings of the (0 1 1) and (1 0 0) crystallographic planes of monoclinic $CoWO_4$ nanoparticles, respectively.

Moreover, the estimated average particle size is calculated from histogram plot as shown in **Figure 4.4 (d)** and found to be approximately 36.88 nm. The combination of polycrystallinity and nanoscale morphology suggests that these materials may exhibit enhanced surface area and unique physicochemical properties, making them suitable for applications in electrocatalytic OER.

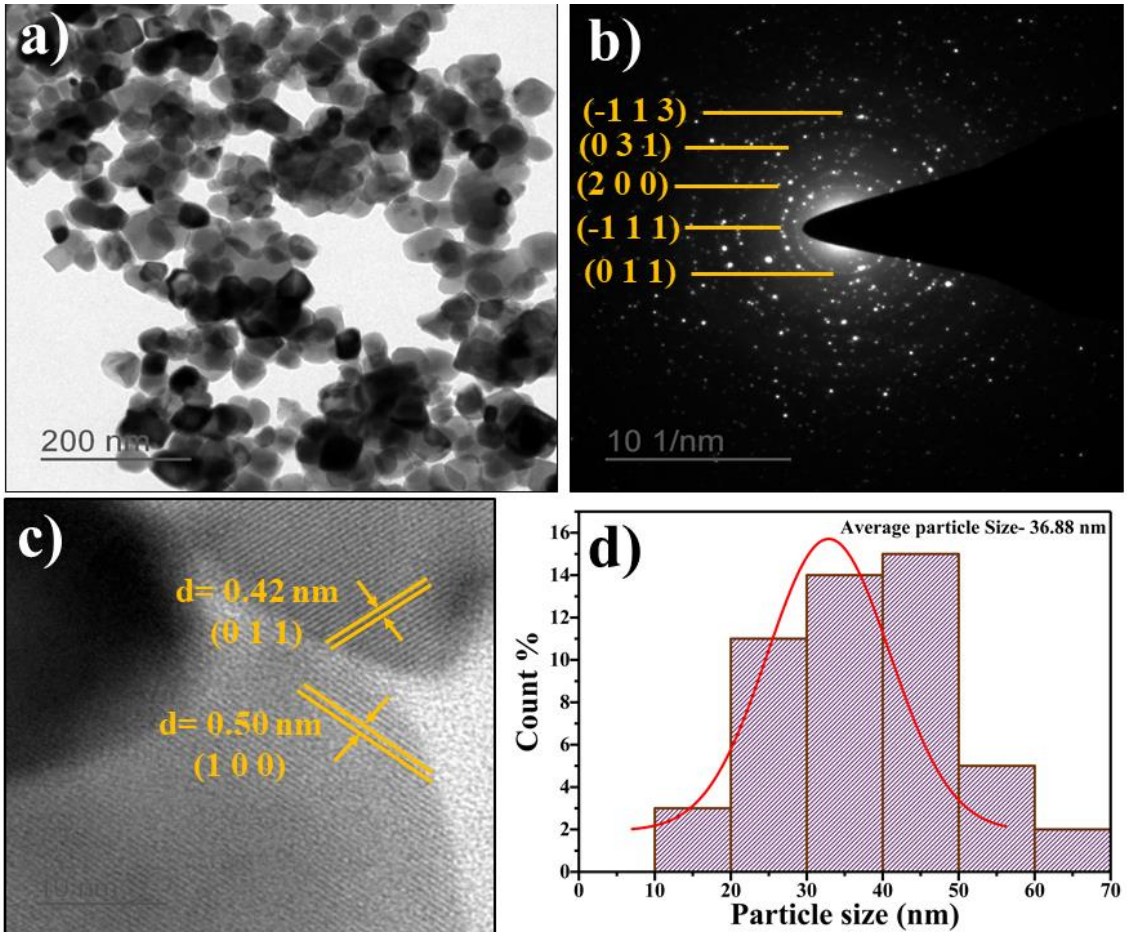

Figure 4.4. a) TEM micrograph of $CoWO_4$ catalyst, **b)** SAED pattern of $CoWO_4$, **c)** HR-TEM micrograph of $CoWO_4$ catalyst, **d)** particle size distribution of $CoWO_4$.

4.5.1.5. XPS

XPS was implemented to analyze the chemical states of surface atoms and elemental composition in the synthesized cobalt tungstate nanoparticles ($CoWO_4$). High-resolution XPS spectra provide deeper insights into the electronic states of the elements. The Co 2p core-level spectra for crystalline $CoWO_4$ **(Figure 4.5 (a))** exhibit two distinct peaks at approximately 780 eV and 796 eV, related to the Co $2p_{3/2}$ and Co $2p_{1/2}$ spin-orbit doublet, respectively. Such

binding energy values are characteristic of the Co^{2+} oxidation state, indicating that cobalt exists predominantly in its divalent state [41]. Furthermore, the presence of satellite peaks at binding energies of 786 eV and 803 eV provides additional confirmation of the existence of cobalt oxide. These findings are consistent with previous reports by S. Rajagopal *et al.* [42].

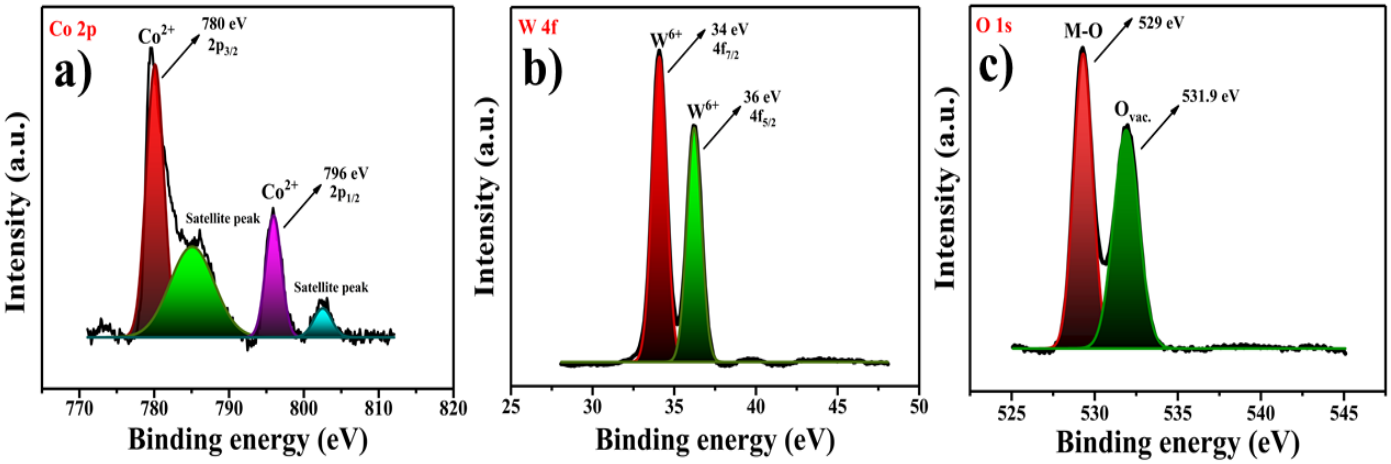

Figure 4.5. High resolution XPS spectra of **a)** Co 2p, **b)** W 4f, **c)** O 1s.

Similarly, the W 4f core-level spectra for $CoWO_4$ **(Figure 4.5 (b))** display two prominent peaks around 34 eV and 36 eV, which is ascribed to the W $4f_{7/2}$ and W $4f_{5/2}$, respectively. This confirms that tungsten is present in its +6 oxidation state, consistent with the expected chemical composition of $CoWO_4$ [42]. The analysis revealed the presence of two distinct types of O^{2-} ions in the synthesized material, denoted as O_I and O_{II}, which were differentiated based on their binding energy positions **(Figure 4.5 (c))**. The O 1s spectrum exhibited a characteristic splitting, where the binding energy of the O_I 1s peak was approximately 3.0 eV more than that of O_{II}. Such a dual peak structure in the O 1s region is commonly observed in metal oxides containing cations with multiple oxidation states. The

observed differences in binding energy suggest that O_{II}^{2-} ions are situated in fully coordinated oxygen environments, where each ion is encased with a complete set of six nearest-neighbor O^{2-} ions. In contrast, O_{I}^{2-} ions are associated with oxygen-deficient regions within the lattice, indicating the presence of oxygen vacancies [43]. The deviation in the comparative intensity of the O_I/O_{II} ratio is directly correlated with changes in the concentration of oxygen vacancies [44]. The observed binding energies confirm the chemical integrity of the material, offering valuable insights into its electronic structure and surface characteristics, which are crucial for its potential applications in catalysis, energy storage, and electronic devices.

4.5.2. Electrochemical characterizations

4.5.2.1. OER study

The electrocatalytic efficiency of prepared cobalt tungstate nanoparticles for OER in alkaline environment was methodically assessed by LSV, CV and EIS measurements. **Figure 4.6 (a)** displays the LSV polarization curves, offering a thorough evaluation of the OER performance across the catalyst series. The overpotential values to obtain current density of 10 mA cm^{-2} (η_{10}) for $Co_{0.5}W_{1.5}O_4$, $CoWO_4$, and $Co_{1.5}W_{0.5}O_4$ were 230 mV, 220 mV and 260 mV, respectively as shown in **Figure 4.6 (c)**. Among the catalysts, the $CoWO_4$ displayed the lowest overpotential demonstrating that this doping level best optimizes the OER catalytic activity. The trend implies that on increasing the tungsten content, the catalytic performance significantly reduces, perhaps owing to variables such as lattice deformation, active site passivation, lower electrical conductivity [45] or a decline in oxygen vacancies [46]. Liu *et al.* performed a thorough investigation on the effect of oxygen vacancies in boosting the OER

performance. Their results demonstrated a substantial link between the concentration of oxygen vacancies and the total catalytic activity of the OER. Specifically, they proved that an increased density of oxygen vacancies greatly enhances the reaction kinetics, leading to greater catalytic efficiency [47]. The fundamental mechanism behind this increase is linked to the electronic changes generated by oxygen vacancies. These defects operate as electron-rich sites, significantly changing the electronic structure of the catalyst and promoting stronger contacts between the catalyst surface and chemical intermediates [48,49].

To ensure a standardized evaluation of catalytic performance, the electrochemical efficacy of the prepared electrocatalysts was examined by determining the specific current density (current density per milligram of the catalyst), as well as the true current density, using the equations, which is already discussed in **Chapter 3 (Equations 3.3** and **3.4)** [50]. These estimates account for changes in material loading and electrode surface roughness, so permitting a more accurate assessment of intrinsic catalytic activity across various samples.

CV measurements, presented in **Figure 4.7**, were employed to extract key electrochemical parameters, including three distinct current densities: apparent current density (j_{app}), true current density (j_{true}), and specific current density (j_{spec}). These estimates, along with the related overpotentials for given current densities along with other kinetic parameters, for all the prepared catalysts, **(Figure 4.8 and 4.9)** are reported in **Table 4.2**. The apparent and true current densities, normalized either by the geometric surface area of the electrode or by the oxide roughness factor, give essential insights into the kinetics of the OER. Such normalization is critical for correctly comparing the catalytic effectiveness of various materials, as it mitigates the effects of morphological variances and electrode roughness on the

measured electrochemical performance. By applying this multi-faceted approach to current density measurement, a more exact knowledge of the intrinsic activity of the catalysts is attained. This technique provides for a reliable assessment of their electrocatalytic potential, permitting the discovery of ideal compositions and structural alterations for better OER efficiency.

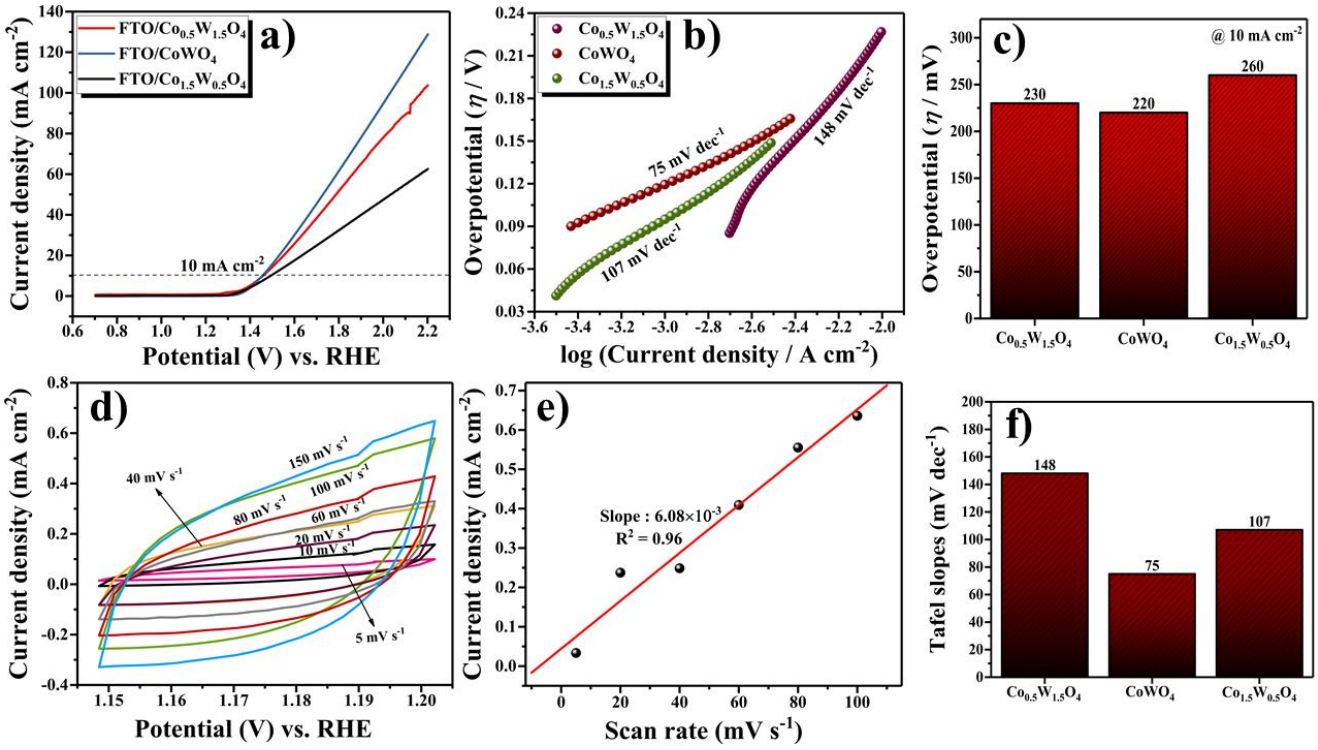

Figure 4.6. (a) LSV curves recorded at a scan rate of 0.5 mV s^{-1} in 1 M KOH at 25 °C, **(b)** Tafel slope analysis of the investigated catalysts, **(c)** comparison of overpotential values for the prepared catalysts, **(d)** CV of the FTO/$CoWO_4$ electrode in the non-faradaic region at varying scan rates, **(e)** corresponding C_{dl} plot for the FTO/$CoWO_4$ electrode, and **(f)** Tafel slope variation across the prepared catalysts.

The kinetics of the OER were determined by Tafel plots, which depict the relationship between overpotential (η) and the logarithm of current density (log j) utilizing analytical Tafel equation (η = b log j) [51]. The Tafel slopes for $Co_{0.5}W_{1.5}O_4$, $CoWO_4$, and $Co_{1.5}W_{0.5}O_4$ as seen in **Figure 4.6 (b)**, have been calculated to be 148 mV dec^{-1}, 75 mV dec^{-1}, and 107 mV dec^{-1} respectively. The values were derived by linear regression of the Tafel plots. A decrease in Tafel slope indicates improved reaction kinetics, signifying more effective charge transfer. Among the analyzed materials, $CoWO_4$ demonstrated the lowest Tafel slope. The enhanced catalytic activity seen with this equal stoichiometric ratio highlights the efficacy of the doping method in modifying the material's electronic characteristics. The comparison of the tafel slopes of prepared cobalt tungstate catalysts are shown in **Figure 4.6 (f)**. Further, this smaller tafel slope along with the lower overpotential and higher current density is validated from Nyquist plots, showing lowest charge transfer resistance amongst the rest of the prepared stoichiometries.

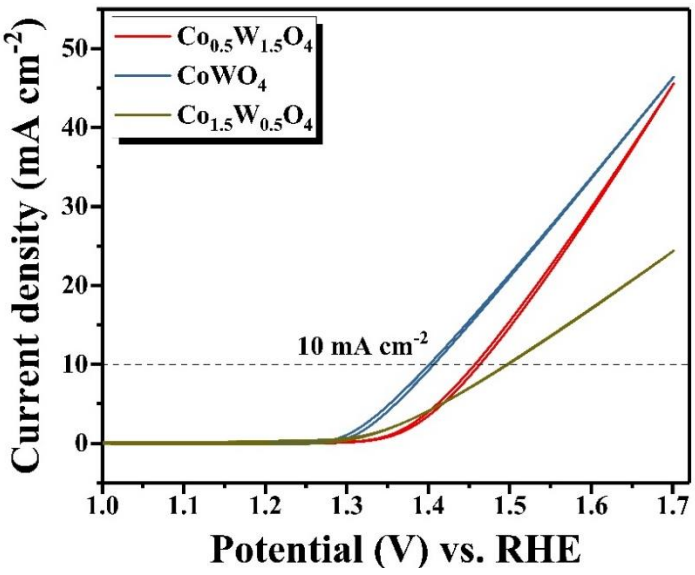

Figure 4.7. CV of prepared catalysts.

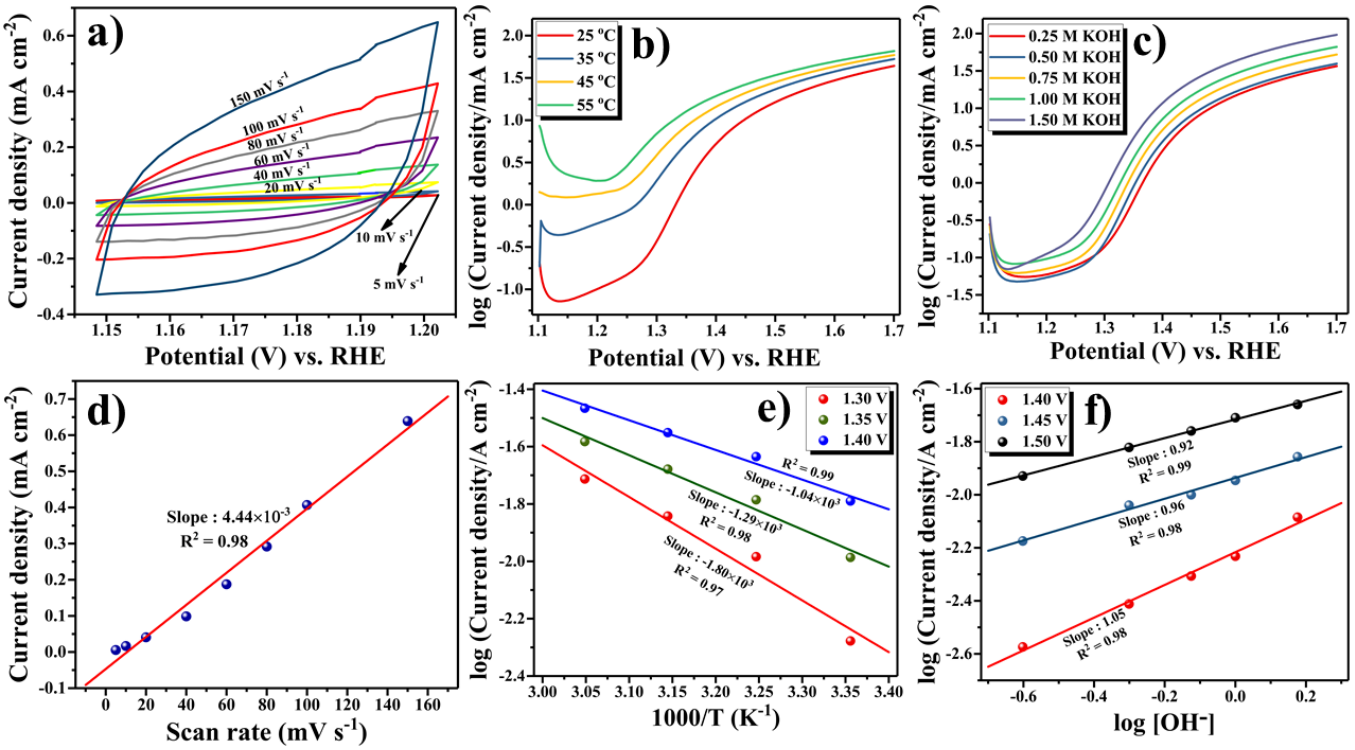

Figure 4.8. $Co_{0.5}W_{1.5}O_4$: a) CV in non-faradaic region at different scan rates, **b)** Tafel polarization curves at different temperatures, **c)** Tafel polarization curves at different concentrations of KOH, **d)** corresponding C_{dl} plot, **e)** corresponding Arrhenius plot, **f)** order of reaction.

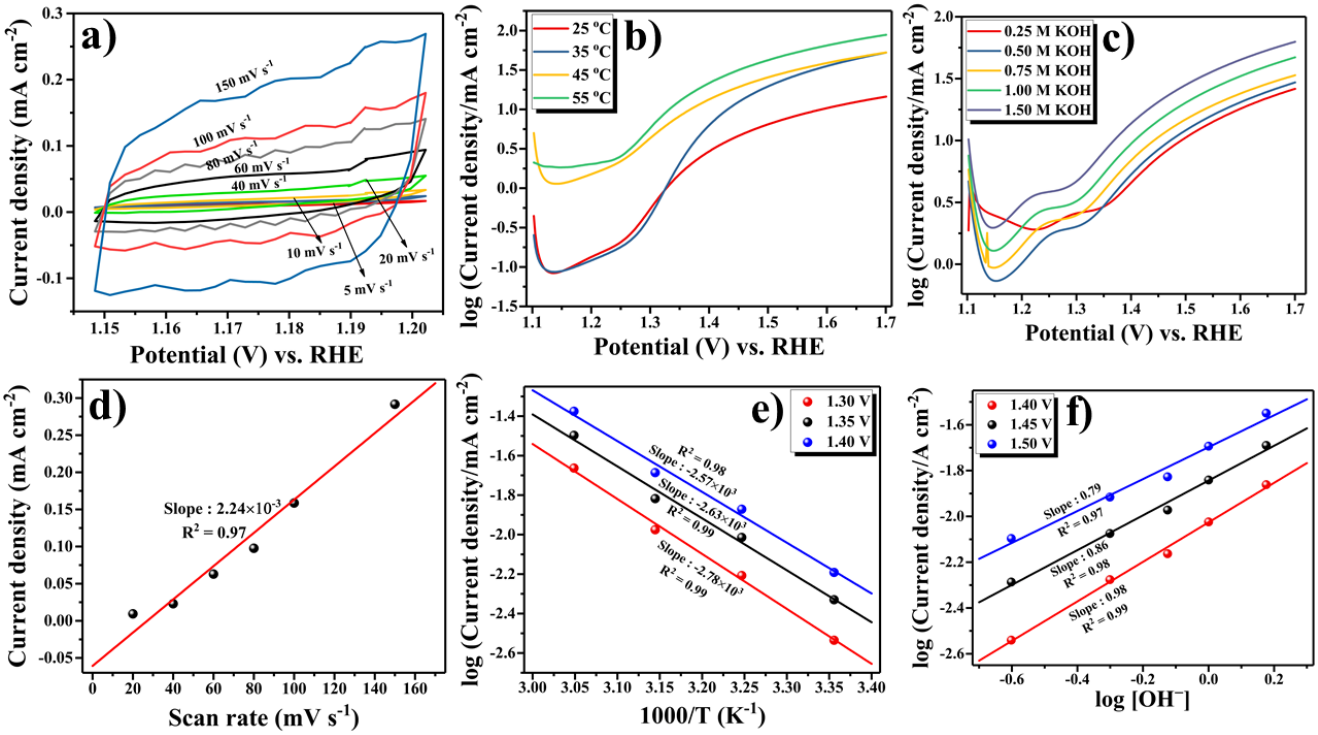

Figure 4.9. $Co_{1.5}W_{0.5}O_4$: a) CV in non-faradaic region at different scan rates, **b)** Tafel polarization curves at different temperatures, **c)** Tafel polarization curves at different concentrations of KOH, **d)** corresponding C_{dl} plot, **e)** corresponding Arrhenius plot, **f)** order of reaction.

Table 4.2. Electrode kinetic parameters

Electrode	Overpotential (mV) at 10 mA cm^{-2}	Current density at E = 1.75 V ($mA\ cm^{-2}$)			C_{dl} ($mF\ cm^{-2}$)	R_f	ECSA (cm^2)	Tafel Slope ($mV\ dec^{-1}$)
		j_{app}	j_{true}	$j_{specific}$				
$FTO/Co_{0.5}W_{1.5}O_4$	230	31.85	0.57	63.70	2.22	55.50	27.75	148
$FTO/CoWO_4$	**220**	**38.47**	**0.51**	**76.94**	**3.04**	**76.00**	**38.00**	**75**
$FTO/Co_{1.5}W_{0.5}O_4$	260	21.36	0.76	42.72	1.12	28.00	14.00	107

The electrochemically active surface area (ECSA) was assessed by evaluating the double-layer capacitance (C_{dl}) within a narrow potential window, ensuring the absence of faradaic contributions. The C_{dl} measurements were conducted by recording CV curves at scan rates ranging from 5 to 150 mV s^{-1} **(Figure 4.6 (d))**. The difference between the anodic and cathodic current densities ($\Delta j = j_a - j_c$) was analyzed, and the resulting values were mapped as a function of the varying scan rates **(Figure 4.6 (e))**. A linear fit was then applied to these data points to determine the slope of the prepared electrodes. The C_{dl} value, which corresponds to half of the slope obtained from this linear relationship, was estimated using the relevant equation **(Equation 3.5)**, which is already discussed in **Chapter 3** [52]. A higher C_{dl} value corresponds to an increased ECSA, which directly correlates with the availability of more

electrochemically active sites. Also, the roughness factor (R_f) gives vital insights into the spatial distribution and accessibility of active sites within a system. The higher R_f value suggests an extended and more favorable adsorption surface, suggesting improved contact between the electrode material and the electrolyte. This parameter is quantitatively calculated using **Equation 1.25 (Chapter 1)** [53]. The ECSA was determined by applying the relevant approaches **(Equation 1.24) (Chapter 1)** and the enhanced performance of the FTO/$CoWO_4$ electrode material, as indicated by a greater ECSA, suggests a larger number of accessible catalytic sites, thereby contributing to improved electrochemical activity **(Figure 4.10 (d))**. These active sites are essential for promoting efficient electron and proton transfer between the electrode and the electrolyte, which significantly influencing the electrochemical reaction dynamics. Additionally, these sites actively participate in the electrolysis process, contributing to overall catalytic performance.

EIS was applied to investigate charge transport kinetics between the electrolyte and the electrode material throughout the electrocatalytic process. Measurements were done at a given potential to determine the charge transfer resistance (R_{ct}) and the solution resistance (R_s) in the low and high-frequency regions, respectively [54]. **Figure 4.10 (a)** depicts Nyquist plots, where the FTO/$CoWO_4$ electrode exhibits a smaller semicircle, suggesting decreased charge transfer resistance (R_{ct}) of 56 **Ω** relative to both derived catalysts. The increased charge transport capabilities of the transition hybrid catalyst may be due to its high electronic conductivity, enabled by the integration of the electrocatalyst with the substrate. This enhanced conductivity facilitates fast electron mobility in the high-frequency region and corresponds well with the Tafel slope study. Notably, the FTO/$CoWO_4$ electrode displays faster reaction

kinetics. The lowered charge transfer resistance further validates the high conductivity and lower resistance for electrolyte ion transport at the electrode interface, significantly enhancing oxygen evolution. The interpretation of the Nyquist plot is conducted using an equivalent circuit model (Randles circuit), as depicted in the inset of **Figure 4.10 (b)**. This model provides a systematic representation of the electrochemical processes occurring at the electrode-electrolyte interface. The model incorporates several key resistance components such, R_s which denotes the solution resistance; R_{ct} which corresponds to the charge transfer resistance at the electrode-electrolyte interface [55,56]. The EIS results align well with the LSV experiments, offering a detailed insight into the electrochemical behavior and catalytic efficiency of the investigated materials.

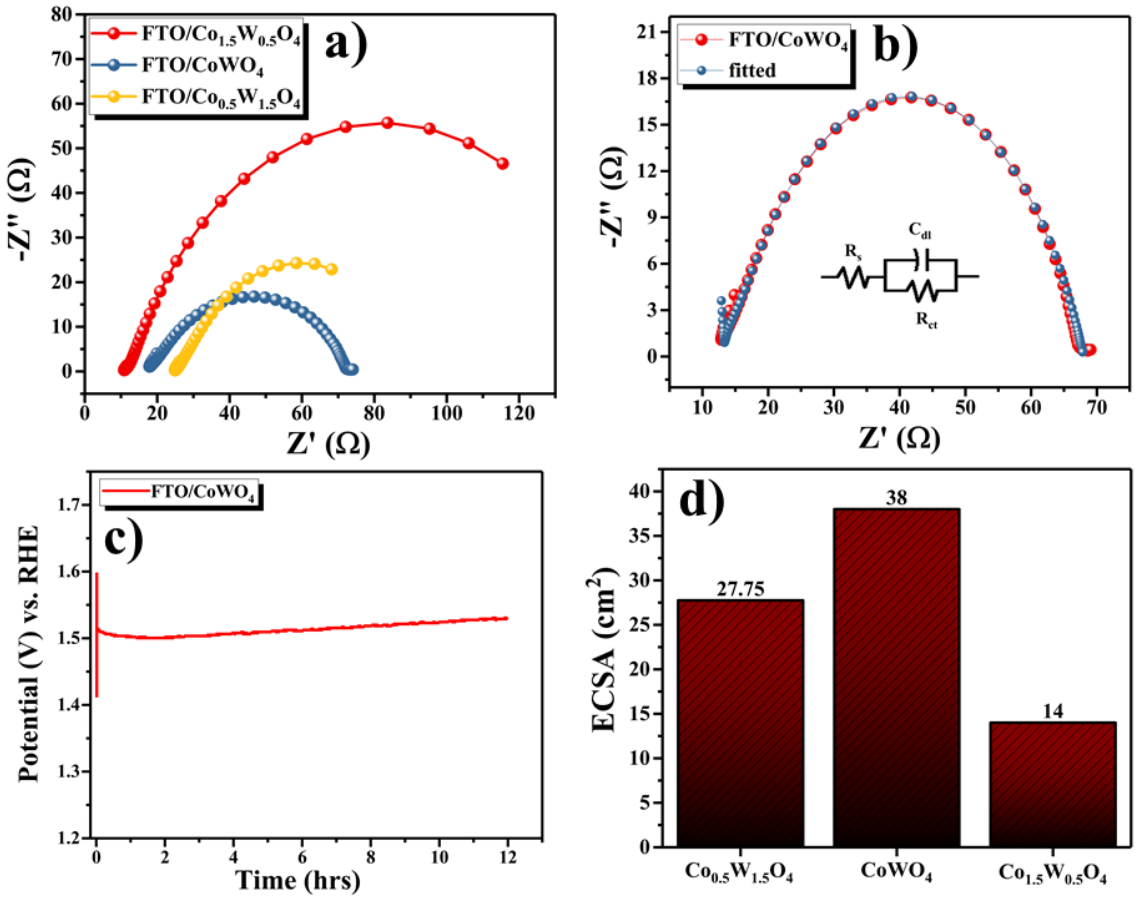

Figure 4.10. **(a)** Nyquist plots, **(b)** fitted Nyquist plot of FTO/$CoWO_4$ electrode, **(c)** chronopotentiometry test of the FTO/$CoWO_4$ electrode, and **(d)** ECSA variation for the synthesized catalysts.

4.5.2.2. Thermodynamic study

The fundamental thermodynamic parameters that govern the electrochemical process were meticulously evaluated through a systematic investigation of electrodes composed of FTO/$Co_xW_{2-x}O_4$. The research sought to ascertain the standard electrochemical activation energy ($\Delta H_{el}^{0\neq}$), the standard entropy of activation ($\Delta S^{0\neq}$), and the standard enthalpy of

activation ($\Delta H^{0\neq}$). During the course of the experiments, the reference electrode was maintained at a constant temperature of 25 °C, while anodic polarization curves were taken in a 1 M KOH electrolyte across a temperature varying from 25 °C to 55 °C **(Figure 4.11 (a))**. Arrhenius plots were meticulously constructed to examine the temperature dependence of the electrochemical reaction **(Figure 4.11 (b))**. A comparative evaluation is presented in **Table 4.3.**

As anticipated, the FTO/$CoWO_4$ electrode exhibited the lowest electrochemical activation energy among the tested materials, signifying that the composite required less energy to initiate and sustain the reaction. This observation highlights the superior catalytic efficiency of the composite material in comparison to other stoichiometries. The transfer coefficient (α) was determined according to **Equation 1.29 (Chapter 1)**. The calculated mean value of α for the FTO/$CoWO_4$ material was determined to be nearly one, suggesting a highly effective charge transfer mechanism.

Additional thermodynamic parameters were obtained through the application of standard equations **(Equations 1.28 and 1.30)**, which is already discussed in **Chapter 1**, with their mean values presented in **Table 4.3**. The Tafel slope (b), expressed in mV dec^{-1}, was obtained from polarization curves measured at increasing temperatures, providing insights into the reaction kinetics. Additionally, Planck's constant (h) and the Boltzmann constant (k_B) were incorporated into the frequency term to obtain k_BT/h, further refining the analysis of activation parameters.

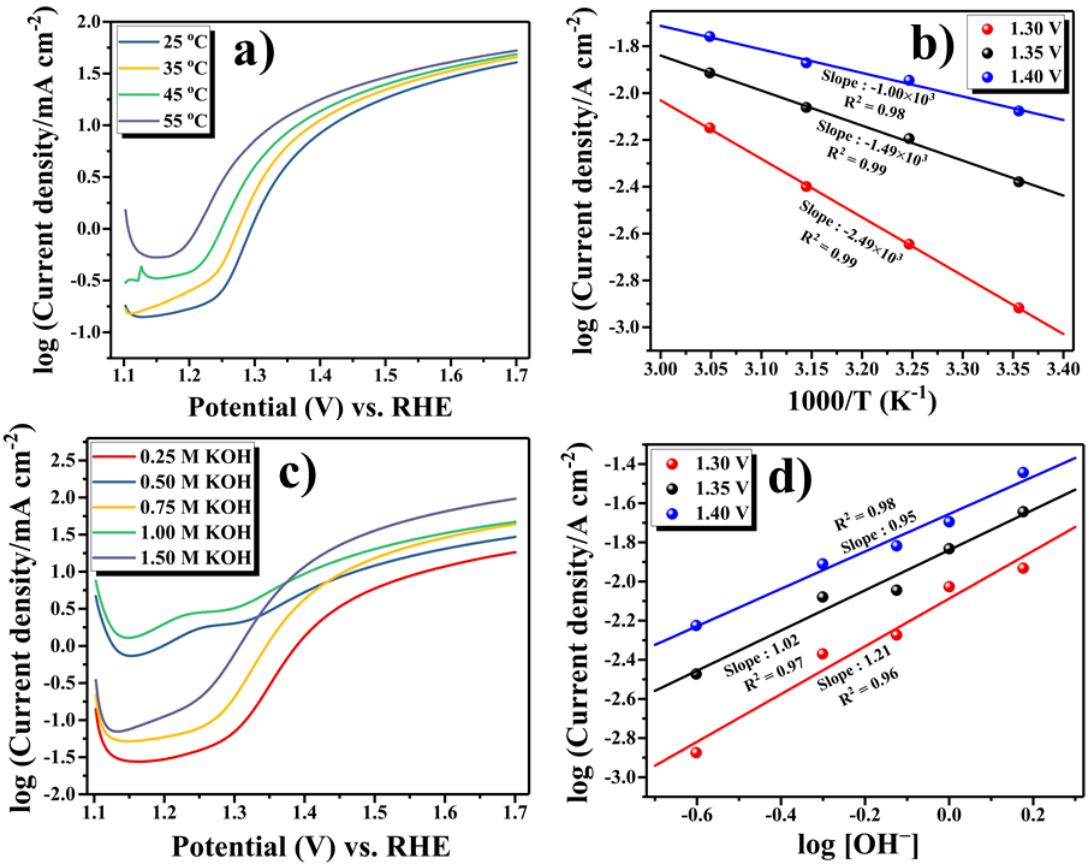

Figure 4.11. (a) Tafel polarization plots of the FTO/$CoWO_4$ electrode at various temperatures, **(b)** corresponding Arrhenius plot, **(c)** Tafel polarization plots of the FTO/$CoWO_4$ electrode at varying KOH concentrations. **(d)** reaction order determination.

The initiation of adsorption during the electrochemical oxygen evolution process is most pronounced for the FTO/$CoWO_4$ electrode, suggesting a higher density of active sites accessible for the adsorption of reactive intermediate species. This observation aligns well with the significantly negative value of $\Delta S^{0\neq}$, which indicates a more ordered transition state and a strong interaction between the electrode surface and the reacting species. The thermodynamic parameters associated with this process are comprehensively presented in **Table 4.3**. These values have been derived following the established methodology detailed in the literature [57],

providing deeper insights into the energetic and entropic aspects governing the electrode's catalytic performance.

Table 4.3. Thermodynamic parameters

Electrode	Standard electrochemical energy of activation ($\Delta H_{el}^{0\neq}$) (kJ mol^{-1})	Standard electrochemical entropy of activation ($-\Delta S_{el}^{0\neq}$) (J K^{-1}mol^{-1})	Transfer coefficient (α)	Standard enthalpy of activation ($\Delta H^{0\neq}$) (kJ mol^{-1})
FTO/$Co_{0.5}W_{1.5}O_4$	19.91	105.56	0.39	26.47
FTO/$CoWO_4$	**19.14**	**108.48**	**0.89**	**32.08**
FTO/$Co_{1.5}W_{0.5}O_4$	49.20	50.88	0.55	58.27

4.5.2.3. Stability and durability

When assessing an electrocatalyst's feasibility for large-scale commercial applications, its operating efficiency and long-term durability under applied current or potential are crucial considerations. Chrono potentiometric experiments were performed in a 1 M KOH electrolyte solution to evaluate the stability of the $CoWO_4$ electrocatalyst. **Figure 4.10 (c)** shows the

chronopotentiometry response (CP) at a constant current density of 10 mA cm^{-2} for 12 hours continuous operation. The findings suggest that FTO/$CoWO_4$ electrode had electrochemical stability which maintained continuous water electrolysis for around 12 hours. CP analysis reveals a small increase in overpotential during the first few hours of operation. This transient rise can be attributed to the accumulation of newly generated oxygen bubbles at the electrode surface, which introduces resistance to charge transfer. To compensate this resistance and maintain reaction kinetics, an additional potential is required until equilibrium is established [58,59]. Once the system reaches a steady-state condition, the FTO/$CoWO_4$ electrode demonstrates remarkable stability, exhibiting only minimal fluctuations in potential over a continuous 12-hour period, as shown in **Figure 4.10 (c)**. This sustained performance highlights the electrode's ability to maintain catalytic activity despite the persistent formation and release of gas bubbles. The consistent electrochemical response suggests that the electrode structure and active sites remain robust, effectively facilitating oxygen evolution while mitigating the adverse effects of bubble-induced resistance. These findings reinforce the potential of FTO/$CoWO_4$ as a durable and efficient electrocatalyst for long-term OER applications.

4.6. OER Mechanism

The reaction order for the OER was determined by systematically varying the hydroxide ion (OH^-) concentration, following the methodologies outlined in the literature [60]. The calculated reaction order values for each catalyst were found to be non-integral, a phenomenon commonly reported in previous studies [61,62]. This deviation from integer values has been attributed to multiple factors, including the complex interplay between OH^- adsorption, the ionization of surface hydroxyl groups [63], and the overall surface coverage by adsorbed

oxygen-containing intermediates formed during electrochemical oxygen evolution under Temkin adsorption conditions [64,65]. To quantify the reaction order, Tafel polarization measurements were conducted on individually prepared electrodes. The study employed KOH concentrations ranging from 0.25 M to 1.25 M, while maintaining a constant ionic strength using KNO_3 as a neutral supporting electrolyte **(Figure 4.11 (c))**. The polarization curves obtained at different KOH concentrations were analyzed by plotting log (current density) against log [OH^-] at various applied potentials **(Figure 4.11 (d))**. The slopes of the resulting linear fits were then determined to establish the reaction order, providing critical insights into the mechanistic aspects of OER on the investigated electrode materials.

The availability of active sites, which are essential for promoting the reaction, is the primary determinant of the OER mechanism for the very effective $CoWO_4$ catalyst. The catalyst's active metal (M) sites are adsorbed with hydroxyl radicals (OH*) in the first step, which causes hydroxide anions (OH^-) to be oxidized via electron transfer to generate M−OH. The formation of M−O species is then followed by the loss of an electron and a proton from M−OH or by the attachment of more hydroxyl radicals. As the reaction proceeds, electron and ion transfer from metal to oxygen species facilitates the oxidation process that produces a metal hydroperoxide intermediate (M−OOH). The catalytic cycle is subsequently maintained by the M−OOH species' subsequent breakdown, which releases molecular oxygen (O_2) and regenerates active M−O sites. This mechanism is already discussed in **Chapter 3**.

$$OH^- + M \rightarrow M + OH^* + e^- \quad \textbf{(3.6)}$$

$$OH^* + OH^- \rightarrow O^* + H_2O + e^- \quad \textbf{(3.7)}$$

$$OH^- + O^* \rightarrow OOH^* + e^- \quad \textbf{(3.8)}$$

$$OH^- + OOH^* \rightarrow O_2 + H_2O + e^- \quad \textbf{(3.9)}$$

Since, it involves continual electron transfer at many stages, the OER process is dynamic by nature. A larger density of defect sites is introduced which greatly enhances the catalyst's surface area and improves the adsorption and desorption of chemical intermediates (M−O, M−OH, and M−OOH). In an alkaline media, this structural advantage speeds up the oxidation process.

This proposed OER mechanism closely aligns with the electrochemical pathway introduced by Bockris [64]. However, it is crucial to recognize the possible presence of alternative reaction pathways, including the Bockris-Otagawa peroxide route and the Krasil'shchikov mechanism [64], which may also contribute to oxygen evolution under specific conditions. In the suggested mechanism, oxygen-containing species, specifically O* and OH*, act as key surface-adsorbed intermediates, playing a critical role in the catalytic process. The transition metal sites, denoted as 'M' (where M corresponds to Co and W), serve as active centers that facilitate electron transfer and intermediate stabilization throughout the reaction.

4.7. Conclusion

In this study, the cobalt tungstate nanoparticles ($Co_xW_{2-x}O_4$) were successfully synthesized using one-pot hydrothermal synthesis. The structural and morphological characteristics of materials were systematically analyzed using XRD, FT-IR, Raman Spectroscopy, HR-TEM, and XPS. These comprehensive methods successfully proven the elemental composition as well as the crystalline nature of the nanoparticles. To evaluate their potential as electrode

materials for OER, the electrochemical characterizations were investigated through CV, LSV, EIS, and Tafel polarization. Comparative electrochemical evaluations revealed that $CoWO_4$ possess significantly higher electrocatalytic activity toward OER in alkaline medium owing to least overpotential of 220 mV (η_{10}). The superior electrochemical performance of $CoWO_4$ can be attributed to its structure, smaller particle size, and narrow particle size distribution, which enhances charge transfer efficiency. This study not only provides valuable perspectives on designing high-performance electrocatalysts for renewable energy applications but also opens avenues for the development of sustainable energy solutions. The enhanced performance and stability of the $Co_xW_{2-x}O_4$ to make it a promising candidate for use in future energy conversion technologies, contributing to the ongoing efforts to address global energy challenges and advance sustainable energy systems.

4.8. References

[1] G. Wang, L. Zhang, J. Zhang, A review of electrode materials for electrochemical supercapacitors, Chem. Soc. Rev. 41 (2012) 797–828. https://doi.org/10.1039/c1cs15060j.

[2] L.S. De Vasconcelos, R. Xu, Z. Xu, J. Zhang, N. Sharma, S.R. Shah, J. Han, X. He, X. Wu, H. Sun, S. Hu, M. Perrin, X. Wang, Y. Liu, F. Lin, Y. Cui, K. Zhao, Chemomechanics of Rechargeable Batteries: Status, Theories, and Perspectives, Chem. Rev. 122 (2022) 13043–13107. https://doi.org/10.1021/ACS.CHEMREV.2C00002/ASSET/IMAGES/LARGE/CR2C00002_0033.JPEG.

[3] C. Largeot, C. Portet, J. Chmiola, P.L. Taberna, Y. Gogotsi, P. Simon, Relation between the ion size and pore size for an electric double-layer capacitor, J. Am. Chem. Soc. 130 (2008) 2730–2731. https://doi.org/10.1021/JA7106178/SUPPL_FILE/JA7106178-FILE003.PDF.

[4] P. Alotto, M. Guarnieri, F. Moro, Redox flow batteries for the storage of renewable energy: A review, Renew. Sustain. Energy Rev. 29 (2014) 325–335. https://doi.org/10.1016/J.RSER.2013.08.001.

[5] X. Zou, Y.Z.-C.S. Reviews, undefined 2015, Noble metal-free hydrogen evolution catalysts for water splitting, Pubs.Rsc.OrgX Zou, Y ZhangChemical Soc. Rev. 2015•pubs.Rsc.Org 44 (2015) 5148. https://doi.org/10.1039/c4cs00448e.

[6] C. Du, L. Yang, F. Yang, G. Cheng, W.L.-A. Catalysis, undefined 2017, Nest-like NiCoP for highly efficient overall water splitting, ACS Publ. Du, L Yang, F Yang, G Cheng, W LuoAcs Catal. 2017•ACS Publ. 7 (2017) 4131–4137. https://doi.org/10.1021/acscatal.7b00662.

[7] P. Zhou, J. He, Y. Zou, Y. Wang, C. Xie, R. Chen, S. Zang, S. Wang, Single-crystalline layered double hydroxides with rich defects and hierarchical structure by mild reduction for enhancing the oxygen evolution reaction, SpringerP Zhou, J He, Y Zou, Y Wang, C Xie, R Chen, S Zang, S WangScience China Chem. 2019•Springer 62 (2019) 1365–1370. https://doi.org/10.1007/s11426-019-9511-x.

[8] Y. Zou, Z. Liu, R. Liu, D. Liu, C. Dong, Y. Wang, S. Wang, Disordered CoFePi nanosheets with rich vacancies as oxygen evolving electrocatalysts: Insight into the local atomic environment, J. Power Sources 427 (2019) 215–222. https://doi.org/10.1016/j.jpowsour.2019.04.077.

[9] D. Yan, R. Chen, Z. Xiao, S. Wang, Engineering the electronic structure of Co 3 O 4 by carbon-doping for efficient overall water splitting, Electrochim. Acta 303 (2019) 316–322. https://doi.org/10.1016/j.electacta.2019.02.091.

[10] Y. Lyu, R. Wang, L. Tao, Y. Zou, H. Zhou, T. Liu, Y. Zhou, J. Huo, S.P. Jiang, J.

Zheng, S. Wang, In-situ evolution of active layers on commercial stainless steel for stable water splitting, Appl. Catal. B Environ. 248 (2019) 277–285. https://doi.org/10.1016/j.apcatb.2019.02.032.

[11] F. Abdelghafar, X. Xu, Z.S.-M.R. Energy, undefined 2022, Designing single-atom catalysts toward improved alkaline hydrogen evolution reaction, Elsevier (n.d.). https://www.sciencedirect.com/science/article/pii/S2666935822000829 (accessed July 31, 2023).

[12] A. Soni, S. Kumar Maurya, M. Malviya, D. Tiwary, Exploring the synergistically enhanced activity of novel α-MnSe/ppy composite for superior OER catalyst in alkaline medium, J. Electroanal. Chem. 972 (2024) 118640. https://doi.org/10.1016/j.jelechem.2024.118640.

[13] M. Louie, A.B.-J. of the A.C. Society, undefined 2013, An investigation of thin-film Ni–Fe oxide catalysts for the electrochemical evolution of oxygen, ACS Publ. Louie, BellJournal Am. Chem. Soc. 2013•ACS Publ. 135 (2013) 12329–12337. https://doi.org/10.1021/ja405351s.

[14] M. Gong, Y. Li, H. Wang, Y. Liang, J.Z. Wu, J. Zhou, J. Wang, T. Regier, F. Wei, H. Dai, An advanced Ni–Fe layered double hydroxide electrocatalyst for water oxidation, ACS Publ. Gong, Y Li, H Wang, Y Liang, JZ Wu, J Zhou, J Wang, T Regier, F Wei, H DaiJournal Am. Chem. Soc. 2013•ACS Publ. 135 (2013) 8452–8455. https://doi.org/10.1021/ja4027715.

[15] F. Luo, Q. Zhang, X. Yu, S. Xiao, Y. Ling, H. Hu, L. Guo, Z. Yang, L. Huang, W. Cai, H. Cheng, Palladium Phosphide as a Stable and Efficient Electrocatalyst for Overall Water Splitting, Angew. Chemie - Int. Ed. 57 (2018) 14862–14867. https://doi.org/10.1002/anie.201810102.

[16] Y. Ling, Z. Yang, Q. Zhang, Y. Zhang, W. Cai, H. Cheng, A self-template synthesis of defect-rich WS2 as a highly efficient electrocatalyst for the hydrogen evolution reaction, Chem. Commun. 54 (2018) 2631–2634. https://doi.org/10.1039/c7cc08962g.

[17] F. Luo, R. Xu, S. Ma, Q. Zhang, H. Hu, K. Qu, S. Xiao, Z. Yang, W. Cai, Engineering oxygen vacancies of cobalt tungstate nanoparticles enable efficient water splitting in alkaline medium, Appl. Catal. B Environ. 259 (2019) 118090. https://doi.org/10.1016/j.apcatb.2019.118090.

[18] S. Tang, Y. Zhou, X. Lu, Z. Chen, Z. Huang, Z. Li, L. Tian, Surface/interface engineering for fabricating hierarchical Ir doped NiMoO4 covered by CoMn layered double hydroxide toward oxygen evolution reaction, J. Alloys Compd. 924 (2022) 166415. https://doi.org/10.1016/j.jallcom.2022.166415.

[19] M. Song, X. Lu, M. Du, Z. Chen, C. Zhu, H. Xu, W. Cheng, W. Zhuang, Z. Li, L. Tian, Electronic and architecture engineering of hammer-shaped Ir-NiMoO4-ZIF for effective oxygen evolution, CrystEngComm 24 (2022) 5995–6000. https://doi.org/10.1039/d2ce00924b.

[20] Q. Zhang, K. Wang, M. Zhang, T. Chen, L. Li, S. Shi, R. Jiang, Electronic structure optimization boosts Pd nanocrystals for ethanol electrooxidation realized by Te doping, CrystEngComm 24 (2022) 5580–5587. https://doi.org/10.1039/d2ce00710j.

[21] Z. Li, X. Xu, X. Lu, C. He, J. Huang, W. Sun, L. Tian, Synergistic coupling of FeNi3 alloy with graphene carbon dots for advanced oxygen evolution reaction electrocatalysis, J. Colloid Interface Sci. 615 (2022) 273–281. https://doi.org/10.1016/j.jcis.2022.01.088.

[22] J. Diao, W. Yuan, Y. Qiu, L. Cheng, X. Guo, A hierarchical oxygen vacancy-rich WO3 with "nanowire-array-on-nanosheet-array" structure for highly efficient oxygen evolution reaction, J. Mater. Chem. A 7 (2019) 6730–6739. https://doi.org/10.1039/c9ta01044k.

[23] Y. Liu, S. Shrestha, W.E. Mustain, Synthesis of nanosize tungsten oxide and its evaluation as an electrocatalyst support for oxygen reduction in acid media, ACS Catal. 2 (2012) 456–463. https://doi.org/10.1021/cs200657w.

[24] T. Meng, Z. Kou, I.S. Amiinu, X. Hong, Q. Li, Y. Tang, Y. Zhao, S. Liu, L. Mai, S. Mu, Electronic Structure Control of Tungsten Oxide Activated by Ni for Ultrahigh-Performance Supercapacitors, Small 14 (2018) 1800381. https://doi.org/10.1002/smll.201800381.

[25] S. Zhao, Y. Kang, M. Liu, B. Wen, Q. Fang, Y. Tang, S. He, X. Ma, M. Liu, Y. Yan, Modulating the electronic structure of nanomaterials to enhance polysulfides confinement for advanced lithium-sulfur batteries, J. Mater. Chem. A 9 (2021) 18927–18946. https://doi.org/10.1039/d1ta02741g.

[26] S.H. Baeck, K.S. Choi, T.F. Jaramillo, G.D. Stucky, E.W. McFarland, Enhancement of photocatalytic and electrochromic properties of electrochemically fabricated mesoporous WO3 thin films, Adv. Mater. 15 (2003) 1269–1273. https://doi.org/10.1002/adma.200304669.

[27] X. Huang, G. Zhao, G. Wang, Sub-nano CoOx attached onto WO3 for efficient photocatalytic and photoelectrochemical water oxidation, J. Mater. Chem. A 5 (2017) 24631–24635. https://doi.org/10.1039/c7ta08734a.

[28] X. Xu, J. Shen, N. Li, M. Ye, Facile synthesis of reduced graphene oxide/CoWO4 nanocomposites with enhanced electrochemical performances for supercapacitors, Electrochim. Acta 150 (2014) 23–34. https://doi.org/10.1016/j.electacta.2014.10.139.

[29] T. Anitha, A.E. Reddy, R. Vinodh, H.J. Kim, Y.R. Cho, Preparation and characterization of CoWO4/CoMn2O4 nanoflakes composites on Ni foam for electrochemical supercapacitor applications, J. Energy Storage 30 (2020) 101483. https://doi.org/10.1016/j.est.2020.101483.

[30] L. Zhen, W.S. Wang, C.Y. Xu, W.Z. Shao, L.C. Qin, A facile hydrothermal route to the large-scale synthesis of CoWO4 nanorods, Mater. Lett. 62 (2008) 1740–1742. https://doi.org/10.1016/j.matlet.2007.09.076.

[31] S.H. Yu, B. Liu, M.S. Mo, J.H. Huang, X.M. Liu, Y.T. Qian, General synthesis of single-crystal tungstate nanorods/nanowires: A facile, low-temperature solution approach, Adv. Funct. Mater. 13 (2003) 639–647. https://doi.org/10.1002/adfm.200304373.

[32] S. Sagadevan, J. Podder, I. Das, Synthesis and characterization of CoWO4 nanoparticles via chemical precipitation technique, J. Mater. Sci. Mater. Electron. 27 (2016) 9885–9890. https://doi.org/10.1007/s10854-016-5057-5.

[33] A. Ammasi, A.P. Munusamy, M. Shkir, F. Maiz, B. Vellingiri, V.R.M. Reddy, W.K. Kim, Synthesis and electrochemical performance of CoWO4 and CoWO4/MWCNT nanocomposites for highly efficient supercapacitor applications, Diam. Relat. Mater. 139 (2023) 110352. https://doi.org/10.1016/j.diamond.2023.110352.

[34] S. Thongtem, S. Wannapop, T. Thongtem, Characterization of CoWO4 nano-particles produced using the spray pyrolysis, Ceram. Int. 35 (2009) 2087–2091. https://doi.org/10.1016/j.ceramint.2008.11.014.

[35] M. Daturi, G. Busca, M.M. Borel, A. Leclaire, P. Piaggio, Vibrational and XRD study of the system CdWO4-CdMoO4, J. Phys. Chem. B 101 (1997) 4358–4369. https://doi.org/10.1021/jp963008x.

[36] M. Crane, R.L. Frost, P.A. Williams, J.T. Kloprogge, Raman spectroscopy of the molybdate minerals chillagite (tungsteinian wulfenite-I4), stolzite, scheelite, wolframite and wulfenite, J. Raman Spectrosc. 33 (2002) 62–66. https://doi.org/10.1002/jrs.820.

[37] E.C. Xiao, M. Liu, Q. Ren, Z. Cao, M. Guo, G. Dou, Z.M. Qi, F. Shi, Phonon characteristics and dielectric properties of a phase pure CoWO4 ceramic, Ceram. Int. 46 (2020) 15705–15708. https://doi.org/10.1016/j.ceramint.2020.03.049.

[38] S.L. González-Cortés, T.C. Xiao, P.M.F.J. Costa, S.M.A. Rodulfo-Baechler, M.L.H. Green, Relevance of the Co1-xNixWO4 wolframite-type mixed oxide compositions on the synthesis and catalytic properties of W-based carbides, J. Mol. Catal. A Chem. 238 (2005) 127–134. https://doi.org/10.1016/j.molcata.2005.05.012.

[39] R.L. Moreira, R.M. Almeida, K.P.F. Siqueira, C.G. Abreu, A. Dias, Optical phonon modes and infrared dielectric properties of monoclinic CoWO4 microcrystals, J. Phys. D. Appl. Phys. 49 (2015) 045305. https://doi.org/10.1088/0022-3727/49/4/045305.

[40] F.A. Alharthi, H.S. Alanazi, A.A. Alsyahi, N. Ahmad, Hydrothermal synthesis, characterization and exploration of photocatalytic activities of polyoxometalate: Ni-cowo4 nanoparticles, Crystals 11 (2021) 456. https://doi.org/10.3390/cryst11050456.

[41] J. Gomez, E.E. Kalu, High-performance binder-free Co-Mn composite oxide supercapacitor electrode, J. Power Sources 230 (2013) 218–224. https://doi.org/10.1016/j.jpowsour.2012.12.069.

[42] S. Rajagopal, D. Nataraj, O.Y. Khyzhun, Y. Djaoued, J. Robichaud, D. Mangalaraj,

Hydrothermal synthesis and electronic properties of FeWO4 and CoWO4 nanostructures, J. Alloys Compd. 493 (2010) 340–345. https://doi.org/10.1016/j.jallcom.2009.12.099.

[43] J.C.C. Fan, J.B. Goodenough, X-ray photoemission spectroscopy studies of Sn-doped indium-oxide films, J. Appl. Phys. 48 (1977) 3524–3531. https://doi.org/10.1063/1.324149.

[44] X. Li, Y. Wang, W. Liu, G. Jiang, C. Zhu, Study of oxygen vacancies′ influence on the lattice parameter in ZnO thin film, Mater. Lett. 85 (2012) 25–28. https://doi.org/10.1016/j.matlet.2012.06.107.

[45] S. Pal, U.P. Azad, A.K. Singh, D. Kumar, R. Prakash, Studies on some spinel oxides based electrocatalysts for oxygen evolution and capacitive applications, Electrochim. Acta 320 (2019) 134584. https://doi.org/10.1016/j.electacta.2019.134584.

[46] R. Xue, L. Zhao, X. Liu, H. Wang, X. Zhu, Y. Xiao, C. Yuan, B. Cao, Z. Chen, T. Li, H. Dai, Enhanced optical, dielectric, and non-Ohmic properties in Ta-doped Bi2/3Cu3Ti4O12 ceramics, Solid State Sci. 150 (2024) 107495. https://doi.org/10.1016/j.solidstatesciences.2024.107495.

[47] S. Peng, F. Gong, L. Li, D. Yu, D. Ji, T. Zhang, Z. Hu, Z. Zhang, S. Chou, Y. Du, S. Ramakrishna, Necklace-like Multishelled Hollow Spinel Oxides with Oxygen Vacancies for Efficient Water Electrolysis, J. Am. Chem. Soc. 140 (2018) 13644–13653. https://doi.org/10.1021/jacs.8b05134.

[48] H. Li, S. Sun, S. Xi, Y. Chen, T. Wang, Y. Du, M. Sherburne, J.W. Ager, A.C. Fisher, Z.J. Xu, Metal-Oxygen Hybridization Determined Activity in Spinel-Based Oxygen Evolution Catalysts: A Case Study of ZnFe2- xCrxO4, Chem. Mater. 30 (2018) 6839–6848. https://doi.org/10.1021/acs.chemmater.8b02871.

[49] H. Zhu, P. Zhang, S. Dai, Recent Advances of Lanthanum-Based Perovskite Oxides for Catalysis, ACS Catal. 5 (2015) 6370–6385. https://doi.org/10.1021/acscatal.5b01667.

[50] A.S. Chaddha, N.K. Singh, M. Malviya, A. Sharma, Birnessite-clay mineral couple in the rock varnish: a nature's electrocatalyst, Sustain. Energy Fuels 6 (2022) 2553–2569. https://doi.org/10.1039/d2se00185c.

[51] Z. Hu, L. Hao, F. Quan, R. Guo, Recent developments of Co3O4-based materials as catalysts for the oxygen evolution reaction, Catal. Sci. Technol. 12 (2022) 436–461. https://doi.org/10.1039/d1cy01688a.

[52] U.J. Awan, M.A. Basit, S.I.A. Shah, J. Yong-Xin, H. Zhifu, Minimized OER overpotential via SILAR-based development of g-C3N4/CdS nanocomposite, Appl. Phys. A Mater. Sci. Process. 129 (2023) 1–15. https://doi.org/10.1007/s00339-023-07105-y.

[53] A. Hojatshamami, Ni-Co and Ni-Fe Catalysts for The Oxygen Evolution Reaction in

Alkaline Water Electrolysis, (2022). https://hdl.handle.net/11250/3042808 (accessed June 23, 2024).

[54] C. Hu, X. Wang, T. Yao, T. Gao, J. Han, X. Zhang, Y. Zhang, P. Xu, B. Song, Enhanced Electrocatalytic Oxygen Evolution Activity by Tuning Both the Oxygen Vacancy and Orbital Occupancy of B-Site Metal Cation in NdNiO3, Adv. Funct. Mater. 29 (2019) 1902449. https://doi.org/10.1002/adfm.201902449.

[55] T. Chen, M. Qian, X. Tong, W. Liao, Y. Fu, H. Dai, Q. Yang, Nanosheet self-assembled NiCoP microflowers as efficient bifunctional catalysts (HER and OER) in alkaline medium, Int. J. Hydrogen Energy 46 (2021) 29889–29895. https://doi.org/10.1016/j.ijhydene.2021.06.121.

[56] K. Bera, A. Karmakar, K. Karthick, S.S. Sankar, S. Kumaravel, R. Madhu, S. Kundu, Enhancement of the OER Kinetics of the Less-Explored α-MnO2 via Nickel Doping Approaches in Alkaline Medium, Inorg. Chem. 60 (2021) 19429–19439. https://doi.org/10.1021/acs.inorgchem.1c03236.

[57] A.S. Chaddha, N.K. Singh, M. Malviya, A. Sharma, Birnessite-clay mineral couple in the rock varnish: a nature's electrocatalyst, Sustain. Energy Fuels 6 (2022) 2553–2569. https://doi.org/10.1039/D2SE00185C.

[58] L.R. Bard, Allen J., Faulkner, Fundamentals and Applications Plasmonics : Fundamentals and Applications, 2001. https://books.google.com/books?hl=en&lr=&id=Sct6EAAAQBAJ&oi=fnd&pg=PR21&ots=QV3mtaJ2QS&sig=WpR4J4YmgS8Ty7LGdhYY4R8tPNI (accessed May 6, 2024).

[59] K.S. Bhat, H.S. Nagaraja, Nickel selenide nanostructures as an electrocatalyst for hydrogen evolution reaction, Int. J. Hydrogen Energy 43 (2018) 19851–19863. https://doi.org/10.1016/j.ijhydene.2018.09.018.

[60] R.N. Singh, N.K. Singh, J.P. Singh, Electrocatalytic properties of new active ternary ferrite film anodes for O2 evolution in alkaline medium, Electrochim. Acta 47 (2002) 3873–3879. https://doi.org/10.1016/S0013-4686(02)00354-7.

[61] F. Švegl, B. Orel, I. Grabec-Švegl, V. Kaučič, Characterization of spinel Co3O4 and Li-doped Co3O4 thin film electrocatalysts prepared by the sol-gel route, Electrochim. Acta 45 (2000) 4359–4371. https://doi.org/10.1016/S0013-4686(00)00543-0.

[62] R.N. Singh, J.F. Koenig, G. Poillerat, P. Chartier, Thin films of CO3O4 and NiCo2O4 prepared by the method of chemical spray pyrolysis for electrocatalysis. Part IV. The electrocatalysis of oxygen reduction, J. Electroanal. Chem. 314 (1991) 241–257. https://doi.org/10.1016/0022-0728(91)85440-Z.

[63] L.I. Krishtalik, Kinetics and mechanism of anodic chlorine and oxygen evolution reactions on transition metal oxide electrodes, Electrochim. Acta 26 (1981) 329–337. https://doi.org/10.1016/0013-4686(81)85019-0.

[64] J.O.M. Bockris, T. Otagawa, Mechanism of oxygen evolution on perovskites, J. Phys. Chem. 87 (1983) 2960–2971. https://doi.org/10.1021/j100238a048.

[65] R.N. Singh, J.F. Koenig, G. Poillerat, P. Chartier, Thin films of CO3O4 and NiCo2O4 prepared by the method of chemical spray pyrolysis for electrocatalysis. Part IV. The electrocatalysis of oxygen reduction, J. Electroanal. Chem. 314 (1991) 241–257. https://doi.org/10.1016/0022-0728(91)85440-Z.